PRX LIFE **2**, 043019 (2024)

Mpemba-Like Sensory Withdrawal Effect

Asawari Pagare and Zhiyue Lu[*]
Department of Chemistry, University of North Carolina-Chapel Hill, North Carolina 27514, USA

(Received 7 June 2024; accepted 20 November 2024; published 17 December 2024)

Biological sensors rely on the temporal dynamics of ligand concentration for signaling. The sensory performance is bounded by the distinguishability between the sensory state transition dynamics under different environmental protocols. This work presents a comprehensive theory to characterize arbitrary transient sensory dynamics of biological sensors. Here the sensory performance is quantified by the Kullback-Leibler (KL) divergence between the probability distributions of the sensor's stochastic paths. We introduce a novel benchmark to assess a sensor's transient sensory performance arbitrarily far from equilibrium. We identify a counterintuitive phenomenon in multistate sensors: while an initial exposure to high ligand concentration may hinder a sensor's sensitivity towards a future concentration up-shift, certain sensors may show a boost in sensitivity if the initial high concentration exposure is followed by a transient resetting at a low concentration environment. The boosted performance exceeds that of a sensor starting from an initially low concentration environment. This effect, reminiscent of a drug withdrawal effect, can be explained by the Markovian dynamics of the multistate sensor, similar to the Markovian Mpemba effect. Moreover, an exhaustive machine learning study of four-state sensors reveals a tight connection between the sensor's performance and the structure of the Markovian graph of its states.

DOI: 10.1103/PRXLife.2.043019

I. INTRODUCTION

Sensory receptors perceive information from external environments and transmit it into the cell via various signaling mechanisms, despite noise due to thermal fluctuations or imperfections [1–4]. A ligand-receptor sensor that reports the level of ligand concentration is a classic example of a biological sensor operating in the stochastic regime. The accuracy of ligand-receptor sensory mechanisms has been intensively studied in the steady-state regime [5–11]. However, recent studies of various biological processes—e.g., the extracellular signal-regulated Kinase (ERK) pathway [12], and NF-kB signaling under inflammatory stimuli [13]—have revealed that cells respond differently to different temporal patterns of external signals [14–17]. Concepts from information science, such as mutual information, Shannon entropy, cross entropy, Kullback-Leibler (KL) divergence, and so on, have been explored and utilized for analyzing the signaling capacity of various biological processes [18–25].

The sensor's states and the transitions among those states may play an important role in information sensing, particularly temporal pattern recognition. As pointed out in Refs. [26–38], even simple ligand-receptor sensors contains more states than bound and unbound states. For example, various metastable configurations of G protein-coupled receptors (GPCRs) were stabilized and revealed by nanobody binding [37]. The sensor's transitions among various configurations may transduce more information to the downstream information sensory network than that of a binary-state sensor. Furthermore, a larger number of states allow for more possible binding and unbinding pathways of the receptor. For example, Deupi and Kobilka use an energy landscape with four states to argue that the sensor may take two different pathways to bind with a ligand [39]. Moreover, various experimental evidences suggest that proteins can be treated as dynamic molecules that interconvert between a small number of active and inactive states [40–42]. Beyond the spatial complexity of the sensor's state space, the sensor's transient dynamics is richer in information compared to the steady states [22–25].

These works on the spatial and temporal complexity of sensor dynamics inspire questions around the performance limitations of sensors of different state space and the corresponding kinetics. For example, a multistate sensor may not necessarily take the same state transition path in the binding process and an unbinding process (see Fig. 1). Thus, its sensory capability for an up-shift and a down-shift of ligand concentrations may be significantly different. A further question that arises is whether a sensor that is sensitive to concentration up-shift can also be sensitive to a down-shift? What are the underlying design principles to ensure sensitivity in both ways? Beyond the stationary regime, how does the transient dynamics of a sensor affect the sensory capability of a sensor? How quick can a sensor recover from a previous exposure to a high or low ligand concentration?

This paper aims to provide a theoretical framework to address the questions listed above. In particular, we ask how the connectivity and transition rates between the various states of a sensor affect its sensory capability. This work defines

---

[*] Contact author: zhiyuelu@unc.edu

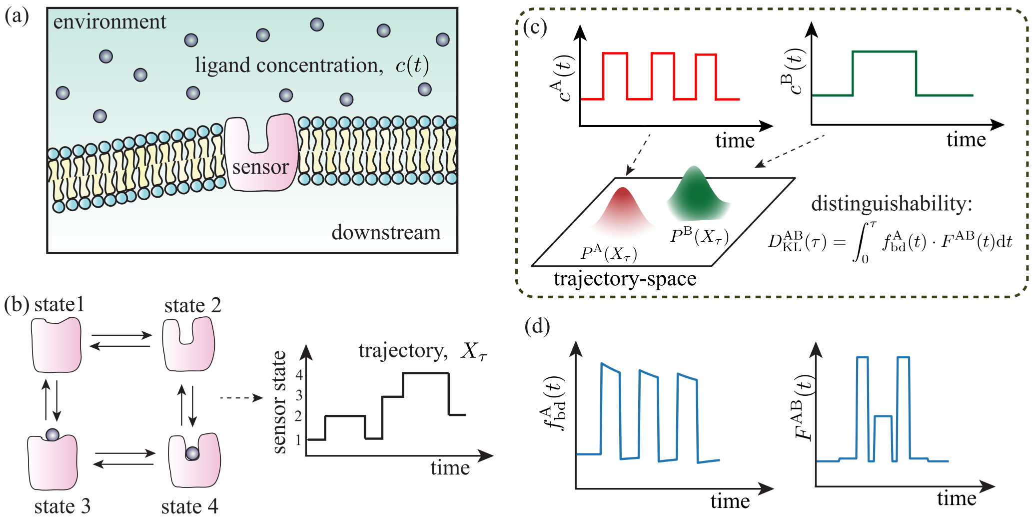

FIG. 1. (a) A ligand-receptor sensor on the surface of a cell probes the environment through binding with ligands and undergoes conformational changes that lead to downstream signaling, (b) a sensor can have multiple bound and unbound states and the temporal trajectory of the sensor's state contains richer information about the environment than in the state probability distribution [22–25], (c) under different temporal patterns of the environmental ligand concentration different ensembles of stochastic trajectories can be observed. The distinguishability between the two ensembles is given by their KL divergence. (d) The KL divergence is shown to be equal to the time integral of the product between the binding frequency, $f_{bd}^A(t)$ weighted by the factor $F^{AB}(t)$ as shown in Eq. (3).

a general formula for the transient sensory upper limit of an arbitrary sensor. When applied to ligand-receptor sensors, we propose benchmark protocols to reveal a sensor's sensory capability as well as the recovery capability. The recovery capability refers to the ability of a sensor to reset its sensory capability after a previous exposure to a high or low ligand concentration environment. Furthermore, this paper identifies a general type of anomalous sensory behavior of ligand-receptor sensors: while an initial exposure to high ligand concentration may hinder a sensor's sensitivity towards a future concentration up-shift, certain sensors may show a boost in sensitivity if the initial high concentration exposure is followed by a transient resetting at a low concentration environment. The boosted performance exceeds that of a sensor starting from an initially low concentration environment. We name this type of behavior a *sensory withdrawal effect*. Finally, we employ machine learning to classify the sensory state graphs based on their structural features, revealing a strong correlation between the sensor's performance, its ability to exhibit the sensory withdrawal effect, and the structure of its Markovian state graph.

This work focuses on analyzing stepwise concentration changes that may addresses several biological scenarios. First, in bacterial chemotaxis, cells must distinguish between increasing and decreasing chemical gradients to determine movement direction. Recent work by Wheeler *et al.* demonstrates that comparing consecutive concentration measurements is crucial for gradient sensing [43]. Second, cellular drug response networks need to differentiate between transient and sustained drug exposures to mount appropriate responses, as exemplified by the p53 system's distinct response patterns to transient versus sustained DNA damage [44]. Third, our framework provides insight into systems exhibiting cellular memory, where previous exposure affects future responses—a phenomenon observed in immune cell priming [45] and bacterial stress responses [46,47]. While these are a few examples of biological events that may be modeled using our theory, this is not an exhaustive list and there may be many more examples in biology related to temporal dynamics. The mutual information rate has traditionally served as a valuable metric for analyzing biological sensors [48], our trajectory-based approach offers distinct advantages: it captures temporal correlations that state-probability-based mutual information might miss, provides direct mechanistic insight into history-dependent sensing, and enables quantification of the "withdrawal effect" we discovered. This approach aligns with recent developments highlighting the importance of trajectory-based information measures in biological systems [22].

II. THEORETICAL FRAMEWORK

A. Stochastic description of sensors

We utilize a Markov state model to capture the state-transition dynamics of an arbitrary sensor. For illustration, a four-state sensor with two bound states and two unbound states is shown by the graph in Figs. 1(a) and 1(b). For any ligand-receptor sensor, we can classify the states into unbound states and various k-bound states. Here k-bound states include a singly bound state ($k = 1$), doubly bound state ($k = 2$), and so on. We assume that the transitions among the unbound states and the transitions among the bound states of same k value all exhibit rates that are independent of the ligand concentration. The binding transitions, from an unbound state to a ($k = 1$)-bound state, or from a k-bound state to a ($k + 1$)-bound state, can be expressed by the product between the ligand concentration and the corresponding transition rate constant. In this paper, we denote the transition rate from state j to state i by R_{ij}.

The sensor, given the external signal of ligand concentration $c(t)$, evolves according to time-dependent transition rates $\{R_{ij}(t)\}$. The stochastic dynamics of a sensor results in state-transition trajectories X_τ that follows the probability distribution $P[X_\tau]$. Here τ denotes the length of the trajectory, which can be considered as the observation time. The ability for the downstream signaling pathway to distinguish temporal patterns of two external signals $c^{\mathrm{A}}(t)$ and $c^{\mathrm{B}}(t)$ via information from the sensor accumulated in the time period τ is thus limited by the distinguishability of the trajectory probabilities, see Fig. 1(c).

B. Transient sensory limit

We propose to use the trajectory Kullback-Leibler (KL) divergence as a universal characterization of a biological sensor's ability to distinguish different temporal patterns of the external signal. By definition, this quantity characterizes the difference between the probability distributions of the sensors' transition pathways under two temporal protocols (two time-dependent signals A and B):

$$D^{\mathrm{AB}}(\tau) \equiv \int \mathcal{D}_{X_\tau} P^A[X_\tau] \ln \frac{P^A[X_\tau]}{P^B[X_\tau]}, \tag{1}$$

where $P^A[X_\tau]$ denotes the probability for a sensor to undergo transition path X_τ within the observation duration τ [see Fig. 1(c)], and the path integral takes all possible stochastic trajectories of the sensor's state into consideration. This quantity serves as an upper limit of the temporal pattern distinguishability information that a sensor could pass to the downstream sensory networks.

According to a recent theory [49], for any transient process that is arbitrarily far from the steady state, the trajectory KL divergence can be expressed as an accumulated weighted sum of all observed transition events

$$D_{\mathrm{KL}}^{\mathrm{AB}}(\tau) = \sum_{\langle x, x'\rangle} \int_0^\tau J_{x'x}^{\mathrm{A}}(t) \cdot F_{x'x}^{\mathrm{AB}}(t)\,\mathrm{d}t, \tag{2}$$

where $J_{x'x}^{\mathrm{A}}(t) = R_{x'x}^{\mathrm{A}}(t) \cdot p^{\mathrm{A}}(x;t)$ is the detailed probability current for the sensor's transition from state x to x' at time t under signal A; the weighting factor $F_{x_k' x_k}^{\mathrm{AB}}(t)$ characterizes the transition rate difference for each transition at time t for the sensor's dynamics under the two signals [see Fig. 1(d)]. In this master equation description, the probability of the sensor being in state x at time t under the protocol A is denoted by $p^{\mathrm{A}}(x;t)$.

For a ligand receptor sensor under two different signals, $c^{\mathrm{A}}(t)$ and $c^{\mathrm{B}}(t)$, their trajectory KL divergence can be significantly simplified into (see Appendix A)

$$D_{\mathrm{KL}}^{\mathrm{AB}}(\tau) = \int_0^\tau f_{\mathrm{bd}}^{\mathrm{A}}(t) \cdot F^{\mathrm{AB}}(t)\mathrm{d}t, \tag{3}$$

where $f_{\mathrm{bd}}^{\mathrm{A}}(t)$ is simply the total ligand binding frequency at time t for the sensor under signal A, and the weighting factor $F^{\mathrm{AB}}(t)$ is a simple function of the ligand concentrations under the two signals at time t:

$$F^{\mathrm{AB}}(t) = \ln \frac{c^{\mathrm{A}}(t)}{c^{\mathrm{B}}(t)} + \frac{c^{\mathrm{B}}(t)}{c^{\mathrm{A}}(t)} - 1. \tag{4}$$

This result implies that, for an arbitrary sensor, the more binding events that likely occur during the time of a large weighting factor $F^{\mathrm{AB}}(t)$ (i.e., large signal difference), the more the sensor can distinguish the two temporal patterns of signals A and B.

In summary, the trajectory KL divergence, especially Eq. (3), provides a convenient and intuitive way to understand the transient sensory capacity of a sensor to discern different temporal patterns of external signal. It leads to intuitive design rules to enhance the distinguishability: the better sensors are those with higher binding event frequencies when the ligand concentration difference between the two protocols are prominent. Moreover, this formula allows us to characterize the transient response of a sensor to arbitrary temporal signals of ligand concentration and to study the sensor's transient response speed and recovery speed when it experiences sudden changes of ligand concentration.

Note that Eqs. (1) and (2) apply to any sensor that senses arbitrary physical quantity, whereas Eqs. (3) and (4) apply to any ligand-receptor sensors. In the next section we develop a benchmark protocol that can be used to study the performance of sensors in sensing a sudden concentration shift.

III. TRANSIENT SENSORY RESPONSES AND BENCHMARK

A. Sensory response: Stationary versus transient

First, the proposed transient theory can be reduced to describe sensors at steady states. Let us start by considering the sensor's stationary difference under constant high and constant low ligand concentrations, c_h and c_l. For two identical copies of a sensor, one at the stationary state of the high ligand concentration c_h and another at the stationary state of the low ligand concentration c_l, they produce two different ensembles of state transition trajectories. The distinguishability between their stochastic trajectories is characterized by a symmetrized KL divergence modified from Eq. (3)

$$D_{\mathrm{ss}}(\tau) = D_{\mathrm{ss}}^{\mathrm{AB}}(\tau) + D_{\mathrm{ss}}^{\mathrm{BA}}(\tau) = \tau \cdot \left(f_{\mathrm{ss}}^{\mathrm{A}} F^{\mathrm{AB}} + f_{\mathrm{ss}}^{\mathrm{B}} F^{\mathrm{BA}}\right), \tag{5}$$

where the $f_{\mathrm{ss}}^{\mathrm{A}}$ denotes the stationary binding event frequency at the stationary concentration c_h and F^{AB} is defined by Eq. (4) with $c^{\mathrm{A}}(t) = c_h$ and $c^{\mathrm{B}}(t) = c_l$. In other words, at the steady state, the sensor's ability to distinguish high and low ligand concentrations can be considered as the product between the observation time τ and a constant information accumulation rate

$$\dot{D}_{\mathrm{ss}} = f_{\mathrm{ss}}^{\mathrm{A}} F^{\mathrm{AB}} + f_{\mathrm{ss}}^{\mathrm{B}} F^{\mathrm{BA}}. \tag{6}$$

This agrees with the intuition that the longer the observation time, the more one can distinguish the two environments.

Then, in this work, we go beyond the steady states and analyze the transient sensory capability of a sensor under the theoretical regime introduced in Sec. II. To simplify the discussion, we focus on a sensor's ability to distinguish a step-wise change of ligand concentration [see Fig. 2(a)]. In

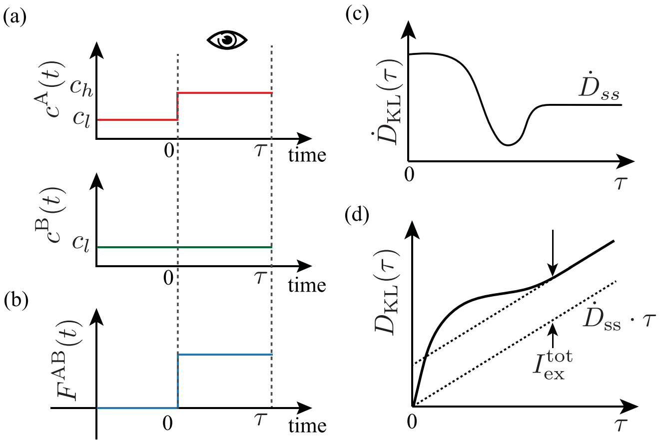

FIG. 2. (a) Protocols to characterize the distinguishability between a step-wise concentration up-shift (protocol A) from a constant concentration (protocol B). (b) The resulting weighting factor. (c) The rate of KL divergence as a function of time. Note that the rate is always positive but not necessarily monotonic; after long-enough time from the initial concentration up-shift, it eventually settles to a constant rate $\dot{D}_{\mathrm{ss}}$. (d) The KL divergence as a function of observation time is monotonic with a positive information accumulation. The difference between the sensor's total accumulated information and the information accumulated under steady state information rate for the same time period defined the total excess information as in Eq. (9).

this case, consider two sensors initialized at the same initial stationary state at concentration c_l. Then at time $t = 0$, one protocol introduces a sudden up-shift of concentration to c_h, whereas the other remains at c_l. The two sensors start to generate distinct trajectory probabilities after time $t = 0$. By utilizing Eq. (3), we can find that the distinguishability between the two protocols, under observation period $(0, \tau)$ becomes a function of observation length τ. This distinguishablibilty increases over τ with an *information accumulation rate*

$$\dot{D}_{\mathrm{KL}}(\tau) = f_{\mathrm{bd}}^{\mathrm{A}}(\tau) F^{\mathrm{AB}} + f_{\mathrm{bd}}^{\mathrm{B}}(\tau) F^{\mathrm{BA}}, \tag{7}$$

where $f_{\mathrm{bd}}^{\mathrm{A}}(\tau)$ and $f_{\mathrm{bd}}^{\mathrm{B}}(\tau)$ are the transient binding frequencies for the two protocols at time τ and the weighting factors F^{AB} and F^{BA} are both positive constants. Figure 2(c) illustrates the positive information accumulation rate as a function of observation length τ. Figure 2(d) illustrates the distinguishability $D_{\mathrm{KL}}(\tau)$, i.e., *accumulated information*, as a function of observation length τ.

Given the above analysis, we can compare a sensor's transient sensory capability with the stationary sensory capability. As illustrated in Fig. 2(c), after a concentration up-shift, the transient response of a sensor may relax to the new steady state, and as a result the information accumulation rate converges to the steady-state information rate [Eq. (6)]:

$$\lim_{\tau\to\infty} \dot{D}_{\mathrm{KL}}(\tau) = \dot{D}_{\mathrm{ss}} \approx \dot{D}_{\mathrm{KL}}(\tau_{\mathrm{ss}}), \tag{8}$$

where τ_{ss} denotes the relaxation time of the sensor. To highlight the difference between the sensor's transient sensory capability and steady-state sensory capability, we define their difference as the *total excess information*

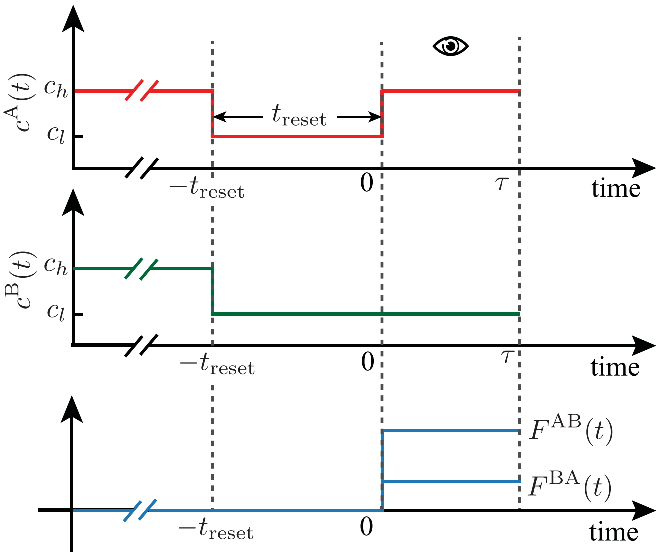

FIG. 3. Benchmark protocols $c^{\mathrm{A}}(t)$ and $c^{\mathrm{B}}(t)$ to capture a sensor's transient response along with its ability to recover from a previous high-concentration exposure.

$$I_{\mathrm{ex}}^{\mathrm{tot}} = \lim_{\tau\to\infty} D_{\mathrm{KL}}(\tau) - D_{\mathrm{ss}}(\tau), \tag{9}$$

as shown in Fig. 2(d). If $I_{\mathrm{ex}}^{\mathrm{tot}} > 0$ then the sensor's transient response to a sudden concentration up-shift is better than the steady-state sensory capability. If $I_{\mathrm{ex}}^{\mathrm{tot}} < 0$, the sensor's transient response is worse than the steady state.

B. Ligand-receptor sensor benchmark

Using the above characterization, we propose a benchmark to capture a sensor's transient sensory capability as well as a its ability to recover from a previous exposure to high/low concentration. To illustrate the need for recovery, consider a sensor that binds strongly to ligands. After being exposed to a high concentration of ligands, it may be poisoned (i.e., stuck at the bound state) and it experiences a low binding frequency f_{bd}. To increase f_{bd} and the sensory capability, a recovery in a low concentration environment may be needed. It would restore the unbound state and allow for higher f_{bd} at the next concentration up-shift.

To design a benchmark that simultaneously captures the two sensory capabilities, we introduce the step-wise protocols $c^{\mathrm{A}}(t)$ and $c^{\mathrm{B}}(t)$ as illustrated by Fig. 3. In the benchmark, both protocols start by initializing the sensor in a high concentration c_h to mimic the effect caused by a previous exposure to a high concentration of ligands. Then at time $t = -t_{\mathrm{reset}}$, both the protocols lower the ligand concentration to c_l for the sensor's recovery. Ultimately, the next up-shift signal starts at time $t = 0$, when the two protocols start to differ: $c^{\mathrm{A}}(t > 0) = c_h$ and $c^{\mathrm{B}}(t > 0) = c_l$. Under this protocol the sensor's trajectory KL divergence starts to accumulate with positive constant weighting factor F^{AB} and F^{BA} as shown in Fig. 3.

Performance function $I_{\mathrm{ex}}^{\mathrm{tot}}(t_{\mathrm{reset}})$. With the proposed benchmark protocols, any ligand-receptor sensor's transient sensory capability $I_{\mathrm{ex}}^{\mathrm{tot}}(t_{\mathrm{reset}})$ and its dependence on the length of

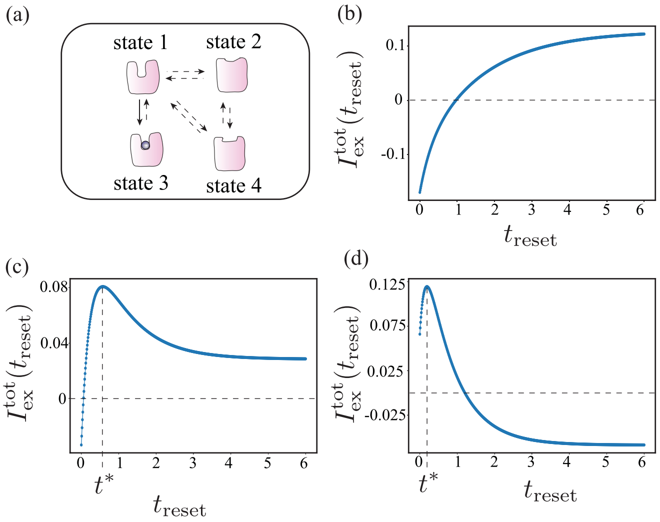

FIG. 4. (a) A four-state sensor with one binding transition andthree unbound states. (b) Sensor's performance improving as $t_{\rm reset}$ increases, as expected by intuition. (c), (d) Sensor performance exhibits nonmonotonicity with respect to $t_{\rm reset}$ indicating a boost of performance at specific values of $t_{\rm reset}$.

resetting time $t_{\rm reset}$ can be studied. This function characterizes the performance of the sensor by capturing both the transient sensory capability and its speed of recovery under resetting periods. A few example performance functions obtained from three different designs of four-state sensors are illustrated in Figs. 4(b), 4(c), and 4(d).

Intuitively, one may expect a sensor's performance function $I^{\rm tot}_{\rm ex}(t_{\rm reset})$ to resemble the curve shown in Fig. 4(b). In this case, the transient sensory performance $I^{\rm tot}_{\rm ex}(0)$ under infinitely short recovery period is lower than that under an infinitely long recovery period $[I^{\rm tot}_{\rm ex}(\infty) \approx I^{\rm tot}_{\rm ex}(\tau_{\rm ss})]$. In other words, the recovery helps the sensor resume the ability to facilitate binding transitions and thus helps the sensor achieve a better transient sensory performance.

For illustrative purposes we denote the performances at the two ends of the performance function as

$$I^{\rm tot}_{{\rm ex},c_h} \equiv I^{\rm tot}_{\rm ex}(0), \tag{10}$$

$$I^{\rm tot}_{{\rm ex},c_l} \equiv I^{\rm tot}_{\rm ex}(\tau_{\rm ss}), \tag{11}$$

where the first one captures a sensor's transient sensory performance when the sensor is initiated at a high-concentration environment (c_h) and the second one captures the sensor's transient sensory capacity if the sensor is initialized at the steady state of a low concentration environment c_l, or equivalently, the sensor is fully recovered at a low concentration environment c_l. Notice that for some sensors, one may observe that its transient sensory performance initiated at high concentration may be better than that of the low concentration, $I^{\rm tot}_{{\rm ex},c_h} > I^{\rm tot}_{{\rm ex},c_l}$, as shown in Fig. 4(d).

Notably, for some sensors the performance function is nonmonotonic with respect to the recovery time, as shown in Figs. 4(c) and 4(d). For these sensors, the curves indicate that the sensors reach a boosted performance for specific $t_{\rm reset}$ values hence uncovering a design principle that can guide sensor performances to their best achievable values. This interesting behavior—the sensory withdrawal effect—of the sensor's transient sensory performance function is a result of the non-stationary dynamics of the sensor traversing different paths of its internal states and is discussed in detail below.

IV. RESULTS

A. Markovian origin of sensory withdrawal effect

One central observation of this work is a counterintuitive withdrawal effect in sensory resetting: a previous exposure to high concentration of ligands followed by a brief period t^* of low concentration can boost a sensor's sensitivity beyond any steady-state behavior. Specifically, for the same sensor under the same long observation time $\tau \gg \tau_{\rm ss}$, the ability for a sensor to distinguish an up-shift ligand concentration becomes the highest under an optimal recovery period $t^* < \tau_{\rm ss}$ Figs. 4(b) to 4(d). Since the recovery does not impact $\dot{D}_{\rm ss}$, this effect can be alternatively characterized in terms of the total excess information: for an optimal resetting period t^*, both $I^{\rm tot}_{\rm ex}(t^*) > I^{\rm tot}_{{\rm ex},c_h}$ and $I^{\rm tot}_{\rm ex}(t^*) > I^{\rm tot}_{{\rm ex},c_l}$ are satisfied, as shown in Figs. 4(c) and 4(d). This effect is a transient nonequilibrium effect due to the time evolution of the system over the complex state space and cannot be explained by traditional steady-state analysis.

This withdrawal effect resembles another nonmonotonic effect found in cooling/heating processes—the Mpemba effect. The Mpemba effect describes that certain systems cool faster if they were previously heated to a higher initial temperature [50–53]. It was shown that the Mpemba effect can be explained by decomposing the temporal evolution of the system into the combination of different eigenmodes. In the decomposition, it can be shown that the cooling time is dictated by the slowest eigenmode, where each mode relaxes under a exponential relaxation at a given rate (determined by the corresponding eigenvalue). The Mpemba effect occurs if the decomposition factor of the slowest relaxation mode nonmonotonically depends on the initial temperature. Here we explain the nonmonotonic withdrawal effect in terms of eigenmode decomposition. At time $t = 0$, the sensor's state probability can be decomposed into a superposition of eigenmodes under the rate matrix corresponding to the constant concentration, c_h or c_l. As proven in Appendix B, each eigenmode (i) contributes a fixed total excess information $m^{\rm A}_i$ and $m^{\rm B}_i$:

$$I^{\rm tot}_{\rm ex}(t_{\rm reset}) = I^{\rm AB}(t_{\rm reset}) + I^{\rm BA}(t_{\rm reset}) \tag{12}$$

$$= \sum_{i=2}^{N} [r^{\rm A}_i(t_{\rm reset}) \cdot m^{\rm A}_i + r^{\rm B}_i(t_{\rm reset}) \cdot m^{\rm B}_i], \tag{13}$$

where the coefficients $r^{\rm A}_i(t_{\rm reset})$ as functions of the resetting time are the decomposition factors of the sensor's initial state into the eigenmodes of the sensor dynamics at a constant ligand concentration c_h. Similarly, $r^{\rm B}_i(t_{\rm reset})$ are the decomposition of the sensor's initial state into the eigenmodes of the dynamics under concentration c_l. For a sensor with the withdrawal effect showing up in both $I^{\rm AB}(t_{\rm reset})$ and $I^{\rm BA}(t_{\rm reset})$ [see Figs. 5(c) and 5(d)], we find two different mechanisms behind the withdrawal effect. One mechanism resembles that found in the Markovian Mpemba effect, but the second

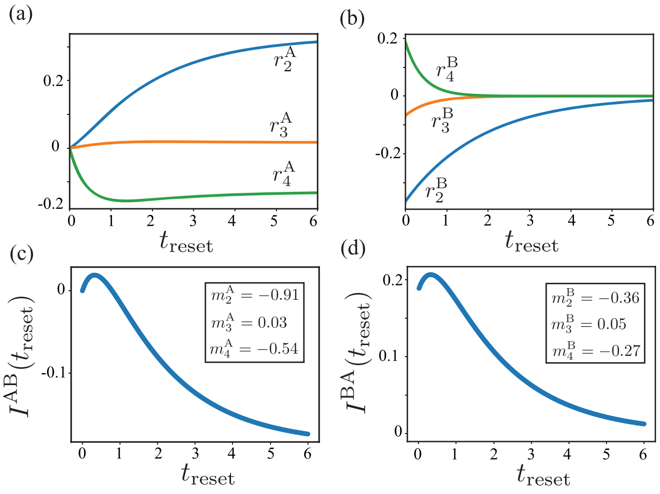

FIG. 5. (a) The coefficients $r_i^A(t_{\rm reset})$, obtained for eigendecomposition of the sensor's initial state at $t = 0$ into the eigenmodes of the sensor dynamics at a constant ligand concentration c_h. (b) The coefficients $r_i^B(t_{\rm reset})$, obtained for eigendecomposition of the sensor's initial state at $t = 0$ into the eigenmodes of the sensor dynamics at a constant ligand concentration c_l. (c), (d) The respective $I^{AB}(t_{\rm reset})$ and $I^{AB}(t_{\rm reset})$ obtained using Eq. (13) with the fixed contributions, m_i^A and m_i^B listed in the insets of (c), (d). These results were obtained for the four-state sensor shown in Fig. 4(a) with the following energy of each states: $E_1 = 0.8$, $E_2 = 0.4$, $E_3 = 0.8$, $E_4 = 0$, and barrier heights between the respective states: $B_{12} = 2$, $B_{13} = 1$, $B_{14} = 1.1$, $B_{24} = 0.5$.

mechanism is novel. In the first case, the withdrawal effect results from the nonmonotonicity of the fourth eigenmode decomposition factor $r_4^A(t_{\rm reset})$ as shown in Fig. 5(a). In the second case, all eigendecomposition factors are monotonic in time, as shown in Fig. 5(b), and the withdrawal effect is a result of the weighted summation of the three monotonic functions. This analysis reveals that the withdrawal effect is a result of more complex dynamical behaviors than the traditional explanation of the Mpemba effect, as it involves the contribution from multiple eigenmodes.

B. Structure origin of sensory withdrawal effect

In the following, we utilize machine learning classification method to systematically investigate the connection between the sensor's state transition graph and the sensory withdrawal effect. Since the distinguishability and the excess information described previously is directly proportional to the average number of binding transitions, we expect sensors with multiple binding transitions to result in better performances.

To characterize the connection between graph structure and the withdrawal effect, we analyze the frequency of observing this effect across all possible four-state transition graphs shown in Fig. 6(a). For each of the 24 distinct transition graphs, we randomly generate 500 different energy landscapes using a uniform distribution, resulting in a comprehensive study of 12 000 possible sensor configurations. As shown in Fig. 6 and Table I, we find a strong correlation between the probability of observing the withdrawal effect and the structural features of the sensor's state graph. Notably, motif 24 in Fig. 6 exhibits a 100% probability of displaying the withdrawal effect.

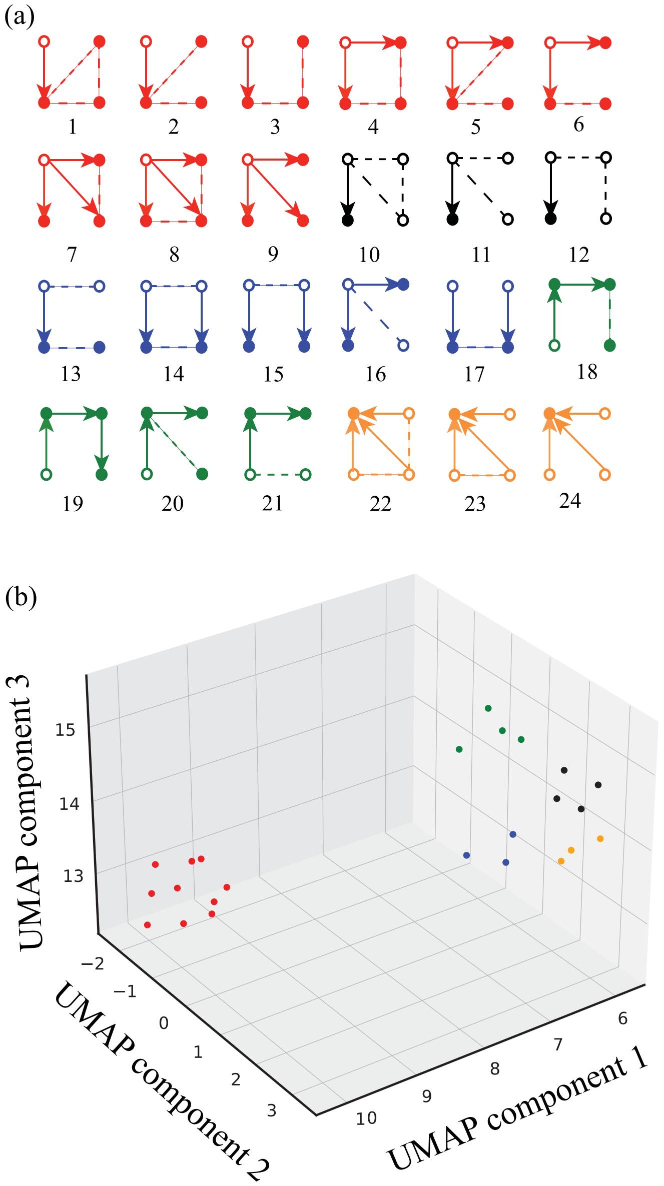

FIG. 6. Four-state sensors classified into five classes based on the features of their graphs. (a) All the four state graphs considered in this study. A solid circle represents a bound state and a hollow circle represents an unbound state. The solid arrows represent a binding transition and the dotted lines represent nonbinding transitions between states. Note that all the transitions are bidirectional. Each graph is colored based on the UMAP cluster as shown in (b).

This 100% occurrence of withdrawal effect for motif 24 can be explained through analysis of the probability evolution over its energy landscape. Consider a case where the energy barrier between states 1 and 3 is high, while the energy barriers between states 1 and 2 and states 1 and 4 are relatively low. Additionally, among the three unbound states, state 3 assumes the lowest energy. Due to the law of mass action, the bound state 1 is favorably occupied at the steady state of high ligand concentrations, while the lowest-energy unbound state 3 is favorably occupied at the steady state of low ligand

TABLE I. For each graph in Fig. 6(a) the percentage of occurrence of the withdrawal effect.

Graph	$w\%$	Graph	$w\%$
1	0	13	1.4
2	0	14	2.8
3	0	15	14.6
4	0	16	42
5	0	17	60.2
6	0	18	0
7	0	19	14
8	0	20	19.8
9	0	21	48.8
10	51.4	22	76.8
11	63.8	23	98.6
12	96.8	24	100

concentrations. Under our benchmark protocol, the system dynamics can be understood in three distinct temporal phases.

In the initial phase ($t < -t_{\mathrm{reset}}$), long exposure to high concentration drives the system toward steady-state abundant occupation of the bound state 1. During the reset phase ($t = -t_{\mathrm{reset}}$ to $t = 0$), when concentration is lowered, states 2 and 4 become populated faster than state 3 due to their differences in energy barriers. For very short resetting time $t_{\mathrm{reset}} \ll 1$, there is insufficient time for the system to leave the bound state 1, leaving the system with low probabilities in the unbound states 2, 3, and 4. For an intermediate (optimal) resetting time $t_{\mathrm{reset}} = t^*$, the system achieves an ideal intermediate distribution where states 2 and 4 are more depopulated than state 3, maximizing the number of rapid binding transitions (from 2 to 1 and from 4 to 1) upon the upcoming phase (increase of ligand concentration at $t = 0$). For a very large resetting time $t_{\mathrm{reset}} \gg 1$, the system fully equilibrates to the low-concentration steady state dominated by state 3, which is kinetically slow to bind with ligands upon the upcoming phase (increase of ligand concentration).

In the subsequent response phase ($t > 0$), the optimal reset time t^* creates a "primed" configuration where states 2 and 4 are significantly occupied to allow rapid new binding events. This unique combination enables a faster response to subsequent concentration increases. The mechanism explains why motif 24 consistently shows the withdrawal effect: its topology enables the necessary separation of timescales between fast transitions (involving states 2 and 4) and slow transitions (involving state 3), while the slow-binding state 3 dominates at the steady state for low concentration.

The analysis of motif 24 can naturally lead to the construction of a minimal system for the withdrawal effect. By removing state 4 while maintaining states 1, 2, and 3 along with their respective energy barriers and transition rates, we can construct a minimal three-state model that exhibits the withdrawal effect. The mechanism remains analogous: state 3 serves as the slow-binding and slow-unbinding memory state while state 2 enables rapid binding and unbinding transitions. Through monotonicity arguments, one can prove that this withdrawal effect cannot occur in any simpler two-state Markov systems, as they lack the necessary capacity for two binding-unbinding pathways with different timescales.

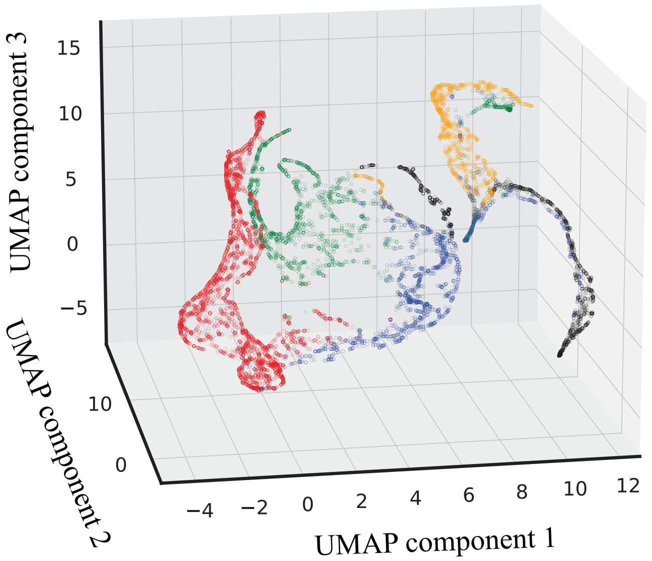

FIG. 7. The clustering of the UMAP embeddings obtained for the performance of sensors show the same five classes as obtained for the graph features confirming a strong correlation between graph features and performance of the sensor.

To capture the structure of the Markov graph we use the following features: the number of unbound states; the number of unbound to unbound transitions; the number of unbound states capable of binding transition; the number of singly bound states not capable of binding; the number of singly bound states capable of binding; the number of singly bound to singly bound transitions—to classify the graphs with uniform manifold approximation and projection (UMAP) embeddings in three dimensions [54]. The clustering of the UMAP embeddings is shown in Fig. 6(b).

The classification of the sensor graph has strong correlation with the occurence of the sensory withdrawal effect. The graphs in classes 2 to 5 show a withdrawal effect with one exception (in class 4) and the graphs in class 1 do not show a withdrawal effect. The features of the graphs in each class and their interpretation are elaborated on in Table II.

C. Correlation between graph features and performance

To systematically investigate the relationship between the sensor's performance and the structure of its state graph, we employ UMAP to visualize the high-dimensional performance data in a three-dimensaionl (3D) latent space. The UMAP representation is generated from four-dimensional vectors capturing key features of the sensor's performance function, $I^{\mathrm{tot}}_{\mathrm{ex}}(t_{\mathrm{reset}})$. These features include the position and value of the maximum $I^{\mathrm{tot}}_{\mathrm{ex}}(t_{\mathrm{reset}})$ within the range (0,1), as well as the ratios of $I^{\mathrm{tot}}_{\mathrm{ex}}$ at the initial ($t_{\mathrm{reset}} = 0$) and final ($t^{\mathrm{max}}_{\mathrm{reset}}$) reset times to the maximum value of $I^{\mathrm{tot}}_{\mathrm{ex}}(t_{\mathrm{reset}})$. Remarkably, the UMAP embeddings of the sensor performances form distinct clusters that precisely match the previously identified graph classifications (Fig. 6), as illustrated by the consistent color coding in Fig. 7. This agreement between the performance-based clustering and the graph classification suggests an inherent link between the sensor's performance

TABLE II. Correlation between graph structure and withdrawal effect.

Class	Withdrawal effect	Graph features	Interpretation
1	No	One unbound state, three bound states. There could be one, two, or three binding transitions.	Since there is only one unbound state the recovery dynamics is too simple to allow for a withdrawal effect.
2	Yes	Three unbound states, one bound state. Only one unbound state is allowed to bind.	Multiple unbound states with only one unbound state allowed for the binding transition. These graphs allow for complex dynamics under the recovery period and thus allow for the withdrawal effect. The less transitions between the unbound states, the stronger the non-monotonicity of its resetting relaxation and thus higher the probability to see the withdrawal effect.
3	Yes	Two unbound states, two bound states.	The stronger the connection (direct or indirect) between the two unbound states, the weaker the withdrawal effect in agreement with class 2.
4	Yes except 1	The only class of graphs that allows for multiple levels of binding ($k > 1$).	No clear trend is observed possibly due to the multiplicity of the bound states ($k > 1$).
5	Yes	Three unbound states, one bound state. All unbound states can make binding transitions.	In agreement with the observation from class 2 and 3, the less connection between the unbound states the more non-monotonicity one could achieve in the recovery period thus allowing for more probability to observe the withdrawal effect.

characteristics and the structural features of its underlying state graph.

To better visualize the correlation between the graph features and the performances of the sensor beyond the withdrawal effect, we plot the performance embeddings separately for each graph in Fig. 8. Clearly, the performance embedding from graphs of the same structural class show similar shapes in the three-dimensioanl latent space. It indicates that the structure of the Markov graph is tightly connected to the information performance of a sensor.

V. DISCUSSION

This paper presents a comprehensive theoretical framework and a systematic benchmark to investigate the transient information sensory performance of ligand-receptor sensors. Through this study, we uncover a counterintuitive phenomenon termed the "sensory withdrawal effect," in which a sensor initially exposed to a high concentration environment, followed by a brief recovery period at low concentration, exhibits a significant enhancement in its sensory performance compared to starting from any stationary ligand concentration level. Our analysis reveals a strong connection between the structure of the sensor's state transition graph and the occurrence of the withdrawal effect, as well as the overall transient information performance. This relationship is robustly confirmed by the consistent classifications of sensors based on their graph features and performance features.

The implications of our findings could extend beyond the realm of theoretical studies and shed light on the mechanisms underlying disease-related mutations in biological receptors. For instance, recent work by Chen, Marsiglia *et al.* [38] on the fibroblast growth factor (FGF) receptor, a receptor tyrosine kinase, reveals how certain mutations in the kinase domain affect its structure and activity. Disease-causing mutations often lead to increased kinase activity, even in the absence of ligand binding and are a major concern in cancer or growth disorders [55–60]. Our theory and the concept of the sensory withdrawal effect may provide a new lens to interpret these findings in the transient dynamics of sensor's state transitions. In the future, our methodology may allow researchers to gain deeper insights into how changes to the receptor state transition graph due to mutations may consequently alter the sensor's performance. This understanding could pave the way for the development of novel therapeutic strategies that target the temporal dynamic of receptors, rather than solely focusing on their static structural features.

Furthermore, our approach could be extended to other receptor systems implicated in various diseases, such as G protein-coupled receptors (GPCRs) [61–64]. By characterizing the transient sensory dynamics of these receptors and identifying potential withdrawal effects, researchers could uncover new mechanisms underlying pathological conditions and guide the design of more effective drug compounds that modulate receptor dynamics.

In conclusion, this work not only advances our fundamental understanding of the complex sensory dynamics in ligand-receptor systems, but also provides a powerful tool for the design and characterization of biosensors with improved transient performances. The insights gained from our study, combined with the growing body of research on disease-related receptor targets, may open up exciting avenues at the interface of theoretical biophysics and medicinal chemistry. The implications of this study have far-reaching consequences for fields such as synthetic biology, drug discovery, and biosensor development.

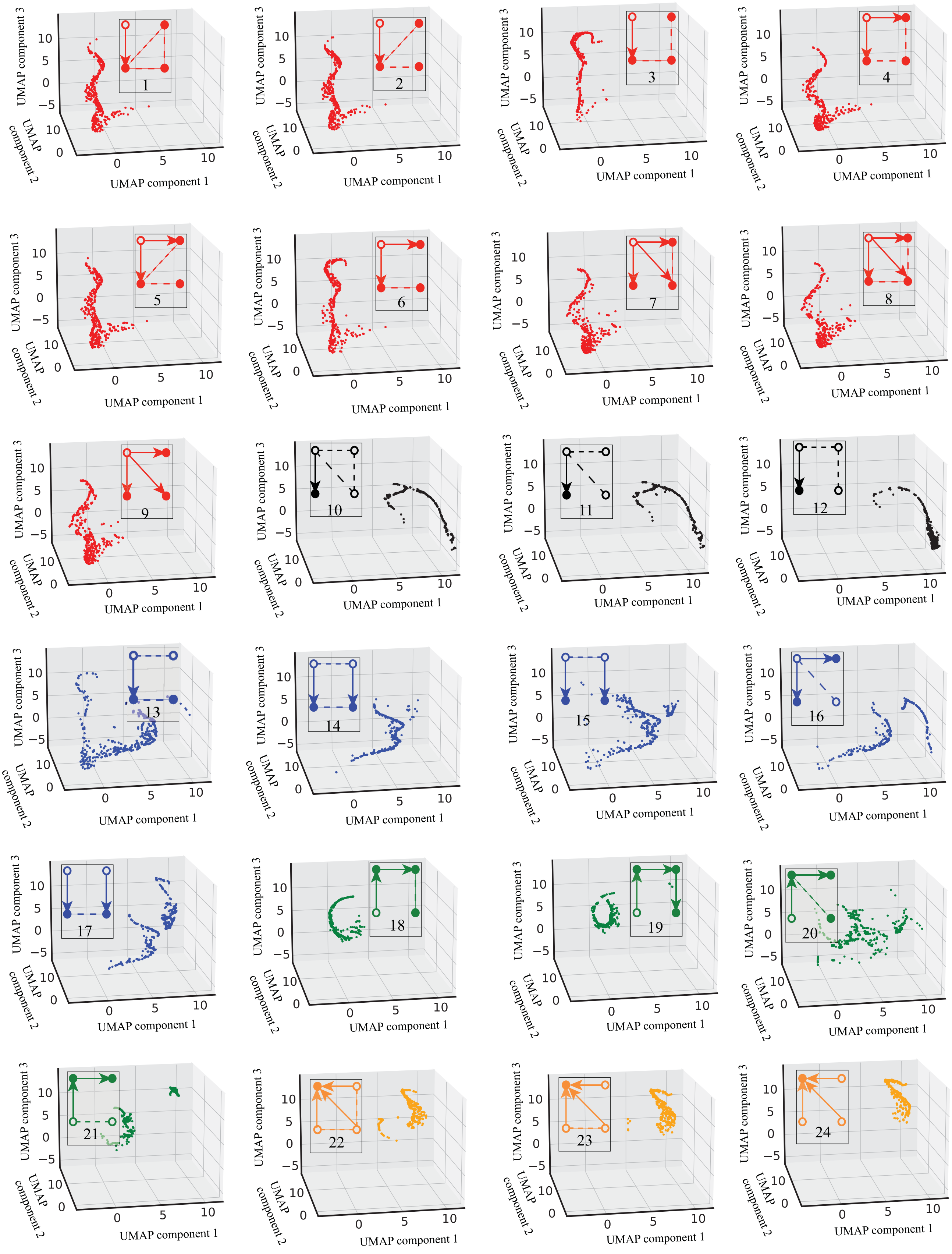

FIG. 8. UMAP embeddings calculated for the performance of all 24 kinds of sensors for 500 energy landscapes each.

The numerical codes written for this study in Julia and Python languages are made publicly available on GitHub: Excess Information at Ref. [65].

ACKNOWLEDGMENTS

The authors appreciate inspiring conversations with Professor Timothy Elston, Profrssor Bryan Roth, and helpful discussions at the workshop "Mathematical Models in Biology: From Information Theory to Thermodynamics" held in 2022 at the Banff International Research Station for Mathematical Innovation and Discovery in Canada. We appreciate valuable suggestions from the reviewers to include the discussion of motif 24 and the discussion of the minimal requirement of the withdrawal effect. This work is financially supported by the National Science Foundation under Grant No. DMR-2145256. The authors also appreciate the Research Computing group at the University of North Carolina at Chapel Hill for providing computational resources and support that have contributed to this work.

APPENDIX A: LIGAND-RECEPTOR SENSOR'S PERFORMANCE EXPRESSED BY BINDING FREQUENCIES

For any transient process that is arbitrarily far from the steady state, the trajectory KL divergence can be expressed as an accumulated weighted sum of all observed transition events as given by Eq. (2). The weighting factor $F^{\rm AB}_{x'x}(t)$ characterizes the transition rate difference for each transition at time t for the sensor's dynamics under the two signals (as given by Eq. (10) in Ref. [49])

$$F^{AB}_{x'x}(t) = \ln \frac{R^A_{x'x}(t)}{R^B_{x'x}(t)} + \frac{R^B_{x'x}(t)}{R^A_{x'x}(t)} - 1 \geqslant 0. \tag{A1}$$

In this description, we adopt the master equation description of the sensor's dynamics, where the transition probability rate from state x to x' is denoted by $R^A_{x'x}(t)$ and the probability of the sensor being in state x at time t under the protocol A is denoted by $p^{\rm A}(x;t)$. For ligand receptor sensors, the external signal is ligand concentration, and it only impacts the probability rates of the binding transitions that have the form

$$R^A_{x'x}(t) = c^A(t)e^{-\beta(B_{x'x}-E_x)}, \tag{A2}$$

where $\beta = 1$ is the inverse temperature, $B_{x'x}$ is the energy barrier between the states x', and x and E_x is the energy of the state x. Thus one can show that the nonbinding transitions do not contribute to the KL divergence [i.e., with a zero weighting factor as shown in Eq. (A1)] and for any binding transition, the weighting factor follows a simple formula as shown in Eq. (4). Ultimately, one can show that for ligand-receptor sensors, the KL divergence is simply a time integral of all binding frequencies weighted by the "transient concentration difference" between the two signal protocols, as shown in Eq. (3).

APPENDIX B: EIGENMODE DECOMPOSITION OF THE TOTAL EXCESS INFORMATION

By using the eigenrepresentation of the sensor's state probability, one can express the initial probability $p^{\rm A}(x,0;t_{\rm reset})$ as the weighted sums of the eigenvectors of the rate matrix $R^{\rm A}$,

$$p(x,t=0;t_{\rm reset}) = \pi^{\rm A}(x) + \sum_{i\geqslant 2} r_i^{\rm A}(t_{\rm reset})v_i^{\rm A}(x,t). \tag{B1}$$

Here the weighting factors are collectively expressed by a vector $r^{\rm A}(t_{\rm reset})$, and the leading eigenvector given by the steady-state distribution $\pi^{\rm A}$. Then as the sensor evolves according to the protocol A, each of its eigenmode exhibits an exponential decay with the decay rate set by the corresponding eigenvalues

$$p^{\rm A}(x,t) = \pi^{\rm A}(x) + \sum_{i\geqslant 2} r_i^{\rm A}(t_{\rm reset})e^{\lambda_i^{\rm A}t}v_i^{\rm A}(x,t), \tag{B2}$$

where $\pi^{\rm A}(x)$ is the steady-state distribution on state x, λ_i is the ith eigenvalue, and $v_i(x,t)$ is the component of the ith eigenvector of matrix $R^{\rm A}$ on state x. Here, the eigenvalues $\{\lambda_i\}$ are ranged in the order $0 = \lambda_1 > \lambda_2 > \lambda_3 \geqslant \cdots \geqslant \lambda_N$.

The KL divergence in Eq. (2) then becomes

$$\begin{aligned} D^{\rm AB}_{\rm KL}(\tau;t_{\rm reset}) = {} & \int_0^\tau {\rm d}t \sum_{\text{edge } x\to x'} R^{\rm A}_{x'x}\pi^A(x)F^{\rm AB}(t) \\ & + \sum_{i\geqslant 2} r_i^{\rm A}(t_{\rm reset}) \int_0^\tau {\rm d}t \sum_{\text{edge } x\to x'} R^{\rm A}_{x'x}e^{\lambda_i^{\rm A}t}v_i^{\rm A}(x,t) \\ & F^{\rm AB}(t), \end{aligned} \tag{B3}$$

where the KL divergence is linearly dependent on the coefficients $\{r_i^{\rm A}\}$. For a time-independent rate matrix $R^{\rm A}$, only the term $e^{\lambda_i^{\rm A}t}$ in Eq. (B3) includes time t. In this case, Eq. (B3) reduces to the following form:

$$\begin{aligned} D^{\rm AB}_{\rm KL}(\tau;t_{\rm reset}) = {} & \sum_{\text{edge } x\to x'} R^{\rm A}_{x'x}\pi^{\rm A}(x)F^{\rm AB}\tau \\ & + \sum_{i\geqslant 2}\Bigg[\frac{r_i^{\rm A}(t_{\rm reset})}{\lambda_i^{\rm A}}\left(e^{\lambda_i^{\rm A}\tau}-1\right) \\ & \times \sum_{\text{edge } x\to x'} R^{\rm A}_{x'x}v_i^{\rm A}(x)F^{\rm AB}\Bigg] \end{aligned} \tag{B4}$$

$$\begin{aligned} = {} & \tau\cdot\left(f^{\rm A}_{\rm ss}F^{\rm AB}\right) + \sum_{i\geqslant 2}\Bigg[\frac{r_i^{\rm A}(t_{\rm reset})}{\lambda_i^{\rm A}}\left(e^{\lambda_i^{\rm A}\tau}-1\right) \\ & \times \sum_{\text{edge } x\to x'} R^{\rm A}_{x'x}v_i^{\rm A}(x)F^{\rm AB}\Bigg]. \end{aligned} \tag{B5}$$

We use a symmetric version of the KL divergence $D_{\rm KL}(\tau) = D^{\rm AB}_{\rm KL}(\tau) + D^{\rm BA}_{\rm KL}(\tau)$ to define the sensor's transient sensory capability in terms of it's total excess information, $I^{\rm tot}_{\rm ex}(t_{\rm reset})$ and its dependence on the length of resetting time $t_{\rm reset}$:

$$I^{\rm tot}_{\rm ex}(t_{\rm reset}) = \lim_{\tau\to\infty} D_{\rm KL}(\tau;t_{\rm reset}) - D_{\rm ss}(\tau;t_{\rm reset}). \tag{B6}$$

Using Eq. (B5), Eq. (B6) for a N state sensor becomes

$$I_{\rm ex}^{\rm tot}(t_{\rm reset}) = \sum_{i\geqslant 2}\left[\frac{-r_i^{\rm A}(t_{\rm reset})}{\lambda_i^{\rm A}}\sum_{{\rm edge}\ x\to x'} R^{\rm A}_{x'x}v_i^{\rm A}(x)F^{\rm AB} + \frac{-r_i^{\rm B}(t_{\rm reset})}{\lambda_i^{\rm B}}\sum_{{\rm edge}\ x\to x'} R^{\rm B}_{x'x}v_i^{\rm B}(x)F^{\rm BA}\right], \tag{B7}$$

which gives Eq. (13) in the main text

$$I_{\rm ex}^{\rm tot}(t_{\rm reset}) = \sum_{i\geqslant 2}\left[r_i^{\rm A}(t_{\rm reset})\cdot m_i^{\rm A} + r_i^{\rm B}(t_{\rm reset})\cdot m_i^{\rm B}\right], \tag{B8}$$

where

$$m_i^{\rm A} = -\frac{1}{\lambda_i^{\rm A}}R^{\rm A}_{x'x}v_i^{\rm A}(x)F^{\rm AB}, \tag{B9}$$

$$m_i^{\rm B} = -\frac{1}{\lambda_i^{\rm B}}R^{\rm B}_{x'x}v_i^{\rm B}(x)F^{\rm BA}. \tag{B10}$$

---

[1] Y. E. Antebi, J. M. Linton, H. Klumpe, B. Bintu, M. Gong, C. Su, R. McCardell, and M. B. Elowitz, Combinatorial signal perception in the BMP pathway, Cell **170**, 1184 (2017).

[2] Y. E. Antebi, N. Nandagopal, and M. B. Elowitz, An operational view of intercellular signaling pathways, Curr. Opin. Syst. Biol. **1**, 16 (2017).

[3] I. Lestas, G. Vinnicombe, and J. Paulsson, Fundamental limits on the suppression of molecular fluctuations, Nature (London) **467**, 174 (2010).

[4] M. Hinczewski and D. Thirumalai, Cellular signaling networks function as generalized Wiener-Kolmogorov filters to suppress noise, Phys. Rev. X **4**, 041017 (2014).

[5] H. C. Berg and E. M. Purcell, Physics of chemoreception, Biophys. J. **20**, 193 (1977).

[6] W. Bialek and S. Setayeshgar, Physical limits to biochemical signaling, Proc. Natl. Acad. Sci. USA **102**, 10040 (2005).

[7] K. Kaizu, W. De Ronde, J. Paijmans, K. Takahashi, F. Tostevin, and P. R. Ten Wolde, The Berg-Purcell limit revisited, Biophys. J. **106**, 976 (2014).

[8] V. Singh and I. Nemenman, Accurate sensing of multiple ligands with a single receptor, arXiv:1506.00288.

[9] H. Nguyen, P. Dayan, and G. Goodhill, How receptor diffusion influences gradient sensing, J. R. Soc. Interface. **12**, 20141097 (2015).

[10] W. Bialek and S. Setayeshgar, Cooperativity, sensitivity, and noise in biochemical signaling, Phys. Rev. Lett. **100**, 258101 (2008).

[11] W. Bialek, Statistical mechanics and sensory signal processing, in *Physics of Biological Systems: From Molecules to Species* (Springer, New York, 1997), pp. 252–280.

[12] C. Marshall, Specificity of receptor tyrosine kinase signaling: Transient versus sustained extracellular signal-regulated kinase activation, Cell **80**, 179 (1995).

[13] A. Hoffmann, A. Levchenko, M. L. Scott, and D. Baltimore, The IκB-NF-κB signaling module: Temporal control and selective gene activation, Science **298**, 1241 (2002).

[14] T. Mora and I. Nemenman, Physical limit to concentration sensing in a changing environment, Phys. Rev. Lett. **123**, 198101 (2019).

[15] J. J. Hopfield, Kinetic proofreading: A new mechanism for reducing errors in biosynthetic processes requiring high specificity, Proc. Natl. Acad. Sci. USA **71**, 4135 (1974).

[16] M. Behar and A. Hoffmann, Understanding the temporal codes of intra-cellular signals, Curr. Opin. Genet. Dev. **20**, 684 (2010).

[17] H. Qian, Reducing intrinsic biochemical noise in cells and its thermodynamic limit, J. Mol. Biol. **362**, 387 (2006).

[18] A. Murugan, D. A. Huse, and S. Leibler, Speed, dissipation, and error in kinetic proofreading, Proc. Natl. Acad. Sci. USA **109**, 12034 (2012).

[19] M. Bauer and W. Bialek, Information bottleneck in molecular sensing, PRX Life **1**, 023005 (2023).

[20] W. Bialek, *Biophysics: Searching for Principles* (Princeton University Press, Princeton, NJ, 2012).

[21] G. D. Potter, T. A. Byrd, A. Mugler, and B. Sun, Dynamic sampling and information encoding in biochemical networks, Biophys. J. **112**, 795 (2017).

[22] Y. Tang, A. Adelaja, F. X.-F. Ye, E. Deeds, R. Wollman, and A. Hoffmann, Quantifying information accumulation encoded in the dynamics of biochemical signaling, Nat. Commun. **12**, 1272 (2021).

[23] S. A. Cepeda-Humerez, J. Ruess, and G. Tkačik, Estimating information in time-varying signals, PLoS Comput. Biol. **15**, e1007290 (2019).

[24] L. Hahn, A. M. Walczak, and T. Mora, Dynamical information synergy in biochemical signaling networks, Phys. Rev. Lett. **131**, 128401 (2023).

[25] A. Pagare, S. H. Min, and Z. Lu, Theoretical upper bound of multiplexing in biological sensory receptors, Phys. Rev. Res. **5**, 023032 (2023).

[26] J. S. Smith, R. J. Lefkowitz, and S. Rajagopal, Biased signalling: From simple switches to allosteric microprocessors, Nat. Rev. Drug Discov. **17**, 243 (2018).

[27] G. G. Gregorio, M. Masureel, D. Hilger, D. S. Terry, M. Juette, H. Zhao, Z. Zhou, J. M. Perez-Aguilar, M. Hauge, S. Mathiasen *et al.*, Single-molecule analysis of ligand efficacy in β_2AR–G-protein activation, Nature (London) **547**, 68 (2017).

[28] Y. Zhang, M. Rózsa, Y. Liang, D. Bushey, Z. Wei, J. Zheng, D. Reep, G. J. Broussard, A. Tsang, G. Tsegaye *et al.*, Fast and sensitive gcamp calcium indicators for imaging neural populations, Nature (London) **615**, 884 (2023).

[29] C. Thomas and R. Tampé, Structure and mechanism of immunoreceptors: New horizons in T cell and B cell receptor biology and beyond, Curr. Opin. Struct. Biol. **80**, 102570 (2023).

[30] F. Han, Y. Chen, Y. Zhu, and Z. Huang, Antigen receptor structure and signaling, Adv. in Immunol. **157**, 1 (2023).

[31] Z. Shen, S. Liu, X. Li, Z. Wan, Y. Mao, C. Chen, and W. Liu, Conformational change within the extracellular domain of B

cell receptor in B cell activation upon antigen binding, eLife **8**, e42271 (2019).
[32] F. De Smet, A. Christopoulos, and P. Carmeliet, Allosteric targeting of receptor tyrosine kinases, Nat. Biotechnol. **32**, 1113 (2014).
[33] S. R. Hubbard and W. T. Miller, Receptor tyrosine kinases: Mechanisms of activation and signaling, Curr. Opin. Cell Biol. **19**, 117 (2007).
[34] N. Volinsky and B. N. Kholodenko, Complexity of receptor tyrosine kinase signal processing, Cold Spring Harbor Perspect. Biol. **5**, a009043 (2013).
[35] W. Sieghart, Allosteric modulation of GABA$_A$ receptors via multiple drug-binding sites, Adv. Pharmacol. **72**, 53 (2015).
[36] L. T. May, K. Leach, P. M. Sexton, and A. Christopoulos, Allosteric modulation of G protein–coupled receptors, Annu. Rev. Pharmacol. Toxicol. **47**, 1 (2007).
[37] T. Che, J. English, B. Krumm, K. Kim, E. Pardon, R. Olsen, S. Wang, S. Zhang, J. Diberto, N. Sciaky *et al.*, Nanobody-enabled monitoring of kappa opioid receptor states, Nat. Commun. **11**, 1145 (2020).
[38] H. Chen, W. M. Marsiglia, M.-K. Cho, Z. Huang, J. Deng, S. P. Blais, W. Gai, S. Bhattacharya, T. A. Neubert, N. J. Traaseth *et al.*, Elucidation of a four-site allosteric network in fibroblast growth factor receptor tyrosine kinases, eLife **6**, e21137 (2017).
[39] X. Deupi and B. K. Kobilka, Energy landscapes as a tool to integrate GPCR structure, dynamics, and function, Physiology **25**, 293 (2010).
[40] T. Xie, T. Saleh, P. Rossi, and C. G. Kalodimos, Conformational states dynamically populated by a kinase determine its function, Science **370**, eabc2754 (2020).
[41] S. S. Taylor and A. P. Kornev, Protein kinases: Evolution of dynamic regulatory proteins, Trends Biochem. Sci. **36**, 65 (2011).
[42] M. Tong and M. A. Seeliger, Targeting conformational plasticity of protein kinases, ACS Chem. Biol. **10**, 190 (2015).
[43] J. H. Wheeler, K. R. Foster, and W. M. Durham, Individual bacterial cells can use spatial sensing of chemical gradients to direct chemotaxis on surfaces, Nat. Microbiol. **9**, 2308 (2024).
[44] E. Batchelor, A. Loewer, C. Mock, and G. Lahav, Stimulus-dependent dynamics of p53 in single cells, Mol. Syst. Biol. **7**, 488 (2011).
[45] M. G. Netea, L. A. Joosten, E. Latz, K. H. Mills, G. Natoli, H. G. Stunnenberg, L. A. O'Neill, and R. J. Xavier, Trained immunity: A program of innate immune memory in health and disease, Science **352**, aaf1098 (2016).
[46] D. M. Wolf, L. Fontaine-Bodin, I. Bischofs, G. Price, J. Keasling, and A. P. Arkin, Memory in microbes: Quantifying history-dependent behavior in a bacterium, PLoS ONE **3**, e1700 (2008).
[47] T. M. Norman, N. D. Lord, J. Paulsson, and R. Losick, Memory and modularity in cell-fate decision making, Nature (London) **503**, 481 (2013).
[48] A. Borst and F. E. Theunissen, Information theory and neural coding, Nat. Neurosci. **2**, 947 (1999).
[49] A. Pagare, Z. Zhang, J. Zheng, and Z. Lu, Stochastic distinguishability of Markovian trajectories, J. Chem. Phys. **160**, 171101 (2024).
[50] E. B. Mpemba and D. G. Osborne, Cool?, Phys. Educ. **4**, 172 (1969).
[51] Z. Lu and O. Raz, Nonequilibrium thermodynamics of the Markovian Mpemba effect and its inverse, Proc. Natl. Acad. Sci. USA **114**, 5083 (2017).
[52] I. Klich, O. Raz, O. Hirschberg, and M. Vucelja, Mpemba index and anomalous relaxation, Phys. Rev. X **9**, 021060 (2019).
[53] S. S. Chittari and Z. Lu, Geometric approach to nonequilibrium hasty shortcuts, J. Chem. Phys. **159**, 084106 (2023).
[54] L. McInnes, J. Healy, and J. Melville, Umap: Uniform manifold approximation and projection for dimension reduction, arXiv:1802.03426.
[55] A. O. Wilkie, Bad bones, absent smell, selfish testes: The pleiotropic consequences of human FGF receptor mutations, Cytokine Growth Factor Rev. **16**, 187 (2005).
[56] M. K. Webster and D. J. Donoghue, FGFR activation in skeletal disorders: Too much of a good thing, Trends Genet. **13**, 178 (1997).
[57] M. R. Passos-Bueno, W. R. Wilcox, E. W. Jabs, A. L. Sertié, L. G. Alonso, and H. Kitoh, Clinical spectrum of fibroblast growth factor receptor mutations, Hum. Mutat. **14**, 115 (1999).
[58] V. Rand, J. Huang, T. Stockwell, S. Ferriera, O. Buzko, S. Levy, D. Busam, K. Li, J. B. Edwards, C. Eberhart *et al.*, Sequence survey of receptor tyrosine kinases reveals mutations in glioblastomas, Proc. Natl. Acad. Sci. USA **102**, 14344 (2005).
[59] P. Pollock, M. Gartside, L. Dejeza, M. Powell, M. A. Mallon, H. Davies, M. Mohammadi, P. Futreal, M. Stratton, J. Trent *et al.*, Frequent activating FGFR2 mutations in endometrial carcinomas parallel germline mutations associated with craniosynostosis and skeletal dysplasia syndromes, Oncogene **26**, 7158 (2007).
[60] G. Grigelioniene, O. Eklöf, E. Laurencikas, B. Ollars, N. Hertel, J. P. Dumanski, and L. Hagenäs, Asn540Lys mutation in fibroblast growth factor receptor 3 and phenotype in hypochondroplasia, Acta Paediatrica **89**, 1072 (2000).
[61] K. L. Pierce, R. T. Premont, and R. J. Lefkowitz, Seven-transmembrane receptors, Nat. Rev. Mol. Cell Biol. **3**, 639 (2002).
[62] R. Lappano and M. Maggiolini, GPCRs and cancer, Acta Pharmacol. Sin. **33**, 351 (2012).
[63] K. Lundstrom, An overview on gpcrs and drug discovery: Structure-based drug design and structural biology on GPCRS, G protein-coupled receptors in drug discovery, in *Methods in Molecular Biology* (Springer, New York, 2009), pp. 51–66.
[64] A. N. Gutierrez and P. H. McDonald, GPCRS: Emerging anticancer drug targets, Cell. Signall. **41**, 65 (2018).
[65] https://github.com/asawari17/Excess_info_and_calculation.